J Adv Ceram

Research Article

# Ultrahigh energy density and efficiency $BaTiO_3$-based multilayer ceramic capacitors

Biao He[1,2], Bin Zhou[1,2], Shiguang Yan[1,✉], Fei Cao[1], Xuefeng Chen[1], Genshui Wang[1,2,3,✉]

Cite this article: He B, Zhou B, Yan S, et al. *J Adv Ceram* 2025, **14**(2): 9221018. https://doi.org/10.26599/JAC.2024.9221018

**ABSTRACT:** Multilayer ceramic capacitors (MLCCs) play a crucial role in pulsed power applications because of their rapid charge/discharge capabilities. However, the combination of high energy density and high efficiency is the main challenge in practical applications. This study presents barium titanate-based ($BaTiO_3$-) lead-free relaxor ferroelectric (RFE) MLCCs formulated with $0.84BaTiO_3$–$0.16Bi(Mg_{0.2}Ni_{0.2}Zn_{0.2}Zr_{0.2}Nb_{0.2})O_3$ (0.84BT–0.16BMNZZN) and platinum inner electrodes via a tape-casting method. The introduction of the high-entropy component BMNZZN effectively enhances the relaxation behavior and local nanodomains while promoting grain refinement, resulting in a comprehensive improvement in insulation performance and energy storage performance. As a result, MLCCs exhibit excellent recoverable energy density ($W_{rec}$ = 15.7 J·cm$^{-3}$) and ultrahigh efficiency ($\eta$) of 96.4% (@1614 kV·cm$^{-1}$), simultaneously showing good temperature stability over a range of –120–100 °C ($W_{rec}$ ≈ 8.9 J·cm$^{-3}$ with a variation of less than ±4.85%, @1078 kV·cm$^{-1}$) and excellent fatigue resistance ($W_{rec}$ ≈ 9.2 J·cm$^{-3}$ with a variation of less than ±0.82% over $10^7$ cycles, and $\eta$ greater than 95%, @1078 kV·cm$^{-1}$). These findings indicate that BT–BMNZZN RFE MLCCs offer a viable solution for high-power energy storage capacitors.

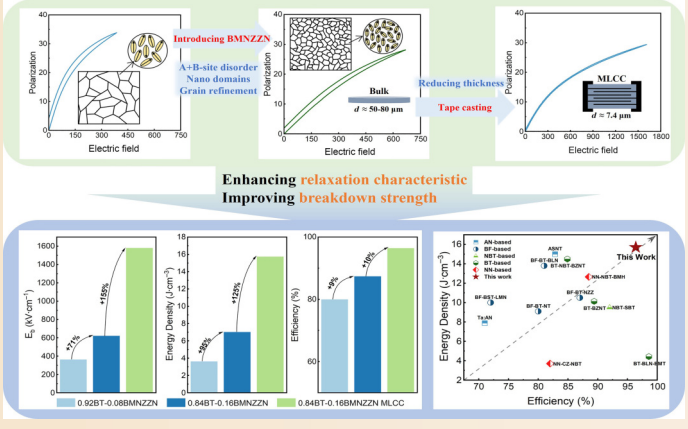


**KEYWORDS:** $BaTiO_3$-based ceramic; energy storage; multilayer ceramic capacitors (MLCCs); high-entropy compound

## 1 Introduction

The diverse applications in various industries, such as aerospace, electric vehicle, and microwave communications, are driving an urgent demand for sustainable and efficient energy storage systems [1–5]. Multilayer ceramic capacitors (MLCCs) are engineered to store electrical energy via an electrostatic field, providing the highest power density, rapid charging/discharging capabilities, superior cyclability, and the highest operating voltage among existing energy storage devices. They are essential in contemporary electrical and electronic systems [6,7]. However, compared with those of electrochemical systems, the relatively low energy storage density of dielectric capacitors limits their broader application. Additionally, to ensure reliability in varying temperature environments, there is a heightened demand for improved energy efficiency and temperature stability. Consequently, ongoing efforts are focused on enhancing energy density and efficiency to support ongoing trends toward miniaturization, integration, and the development of environmentally friendly advanced devices [8–10].

According to electrostatics, the overall energy storage density ($W_{total}$), recoverable energy density ($W_{rec}$), and efficiency ($\eta$) of dielectric capacitors can be determined via the following equations: $W_{total} = \int_0^{P_{max}} E dP$, $W_{rec} = \int_{P_r}^{P_{max}} E dP$, and $\eta = W_{rec}/W_{total} \times 100\%$, where $E$, $P_{max}$, and $P_r$ represent the applied electric field, the maximum polarization, and the remnant polarization, respectively. Consequently, high maximum polarization, high breakdown strength ($E_b$), and minimal hysteresis are advantageous for achieving high $W_{rec}$ and $\eta$. Relaxor ferroelectrics have superior potential and appear to be promising alternatives for energy storage applications because of their synergistically high saturated polarization ($P_s$), low remnant polarization, high breakdown strength, and ultraslim $P$-$E$ loops. Numerous studies have focused on environmentally friendly $BaTiO_3$–$Bi(Me)O_3$ compositions, where Me can be a single or two cations with an average valence of +3. $Bi(Me)O_3$ is selected as an

[1] Key Laboratory of Inorganic Functional Materials and Devices, Shanghai Institute of Ceramics, Chinese Academy of Sciences, Shanghai 200050, China. [2] Center of Materials Science and Optoelectronics Engineering, University of Chinese Academy of Sciences, Beijing 100049, China. [3] The State Key Laboratory of High Performance Ceramics and Superfine Microstructure, Shanghai Institute of Ceramics, Chinese Academy of Sciences, Shanghai 200050, China.

✉ Corresponding authors. E-mail: S. Yan, sicysg@mail.sic.ac.cn; G. Wang, genshuiwang@mail.sic.ac.cn

Received: August 16, 2024; Revised: November 27, 2024; Accepted: December 13, 2024

additive to destroy the long-range ferroelectric order and form polar nanoregions (PNRs) to improve its relaxation characteristics. Relaxor ferroelectrics typically exhibit a temperature-insensitive dielectric constant plateau, which is highly important for achieving thermally stable energy storage. For example, the $0.9BaTiO_3$–$0.1Bi(Mg_{1/2}Hf_{1/2})O_3$ ceramics prepared by Liu *et al.* [11] demonstrated $W_{rec}$ of 3.38 J·cm$^{-3}$ and $\eta$ of approximately 87% at an electric field of 240 kV·cm$^{-1}$. Li *et al.* [12] obtained $0.88BaTiO_3$–$0.12(1-x)Bi(Li_{0.5}Nb_{0.5})O_3$–$0.12xBi(Mg_{0.5}Ti_{0.5})O_3$ MLCCs with $W_{rec}$ of 4.42 J·cm$^{-3}$ and $\eta$ of 98.6% at 500 kV·cm$^{-1}$. Zhao *et al.* [13] obtained $0.87BaTiO_3$–$0.13Bi(Zn_{2/3}(Nb_{0.85}Ta_{0.15})_{1/3})O_3$ MLCCs with $W_{rec}$ of 10.12 J·cm$^{-3}$ and $\eta$ of 89.4% at 1046 kV·cm$^{-1}$ and further improved the energy storage performance by introducing $SiO_2$ to construct a core–shell structure with $W_{rec}$ of 18.2 J·cm$^{-3}$ and $\eta$ of 94.5% at 1755 kV·cm$^{-1}$ [14]. Despite these advancements, achieving both high $W_{rec}$ and $\eta$ in the $BaTiO_3$–$Bi(Me)O_3$ system remains challenging in MLCCs. In the past decade, the application of the high-entropy strategy in energy storage ceramics has attracted widespread attention. High-entropy compounds usually have more than four cations occupying the same site in an equal molar ratio. Owing to the mismatch of mass, radii and bonding states of multiple ions, the lattice is severely distorted, and the atomic arrangement is highly disordered, resulting in strong relaxation behavior and high breakdown strength [15,16]. Qiao *et al.* [17] achieved giant $W_{rec}$ of 7.16 J·cm$^{-3}$ and high $\eta$ of 93.3% by introducing a high-entropy component, $Ba(Zr_{0.2}Ti_{0.2}Sn_{0.2}Hf_{0.2}Nb_{0.2})O_3$, into a $0.65Bi_{0.5}Na_{0.5}TiO_3$–$0.35SrTiO_3$ matrix. Inspired by this, the use of a high-entropy strategy to construct Bi-based high-entropy components instead of traditional $Bi(Me)O_3$ components is expected to broaden the composition design range of the $BaTiO_3$–$Bi(Me)O_3$ material system and further improve its energy storage performance.

Guided by this strategy, a new high-entropy component, $Bi(Mg_{0.2}Ni_{0.2}Zn_{0.2}Zr_{0.2}Nb_{0.2})O_3$ (BMNZZN), was introduced into $BaTiO_3$ (BT) to form a solid solution by considering charge balance and ionic radius compatibility. Compared with binary systems, such as $Bi(Mg_{2/3}Nb_{1/3})O_3$ and $Bi(Mg_{1/2}Hf_{1/2})O_3$, BMNZZN results in greater disparities in terms of local chemical disorder and ionic size, inducing strong relaxor behavior in the BT matrix. This integration results in an exceptional recoverable energy density of 15.7 J·cm$^{-3}$ with high efficiency of 96.4% and a substantial breakdown strength of approximately 1580 kV·cm$^{-1}$ in the 0.84BT–0.16BMNZZN MLCCs. Notably, the energy storage properties exhibit excellent thermal stability, with variations within ±4.85% across a temperature range of −120–100 °C at 1078 kV·cm$^{-1}$, underscoring the potential of the BT–BMNZZN MLCCs for high-energy storage applications.

## 2 Experimental

$(1-x)BaTiO_3$–$xBi(Mg_{0.2}Ni_{0.2}Zn_{0.2}Zr_{0.2}Nb_{0.2})O_3$ (abbreviated as $(1-x)$BT–$x$BMNZZN; $x$ = 0.08, 0.12, 0.16, and 0.20) powders were prepared through a conventional sintering method. The starting materials, including $BaCO_3$ (98.06%), $TiO_2$ (99.8%), $Bi_2O_3$ (99.9%), MgO (99.968%), NiO (98%), ZnO (99.9%), $ZrO_2$ (99%), and $Nb_2O_5$ (99.99%), were mixed and subjected to ball milling with $ZrO_2$ balls for 4 h in anhydrous ethanol. The resulting dried powders were calcined at 950 °C for 2 h. The powders were further milled using smaller $ZrO_2$ balls (1 mm diameter) to achieve a fine particle size. The calcined powders were then pressed into pellets with a diameter of 13 mm and sintered at temperatures ranging from 1130 to 1200 °C for 2 h to achieve densification.

The same powder was employed in the production of MLCCs. The weighed powders, along with the dispersant, binder, and plasticizer, were subjected to milling with $ZrO_2$ balls for 10 h. The slurry was subsequently used to create continuous 0.84BT–0.16BMNZZN tapes with a thickness of approximately 10 μm via tape casting. The same powder was employed in the production of MLCCs. The weighed powders, along with dispersant, binder, and plasticizer, were subjected to milling with zirconia balls for 10 h. The slurry was subsequently used to create continuous 0.84BT–0.16BMNZZN tapes with a thickness of approximately 10 μm via tape casting. Ceramic tapes, screen-printed with Pt paste as the inner electrode, were stacked and aligned with precision via hot isostatic lamination. The resulting MLCCs were sintered at 1100 °C for 3 h.

The crystal structures of the bulk ceramics were analyzed via a powder X-ray diffractometer (XRD; D/max-2550 V, Rigaku, Japan) with Cu Kα radiation ($\lambda$ = 1.5406 Å), and Rietveld refinement analyses were conducted with the GSAS-II software. Raman spectra were acquired via a Raman spectrometer (Renishaw in Via, UK). The microstructures and elemental distributions of the ceramics and MLCCs were characterized via a field emission scanning electron microscope (FE-SEM; Magellan 400, FEI, USA). Transmission electron microscopy (TEM) was performed via a field-emission transmission electron microscope (FE-TEM; JEM-2100F, JEOL, Japan). High-angle annular dark-field (HAADF) imaging was carried out on a Cs-corrected microscope (HF5000, Hitachi, Japan). The domain response was investigated via a commercial atomic force microscope (AFM) system (Jupiter XR, Oxford, UK). The temperature- and frequency-dependent dielectric properties and complex impedance were examined with a broadband dielectric spectrometer (Concept 80, Novocontrol GmbH, Germany). *P*–*E* loops were obtained via a ferroelectric measuring system (TF Analyzer 2000E, aixACCT, Germany). The size of the ceramic sample was approximately 0.05 mm (thickness) × 0.636 mm$^2$ (Au electrode area). The size of the MLCCs sample is approximately 7.4 μm (thickness) × 3.24 mm$^2$ (Pt electrode area). The underdamped and overdamped charge–discharge data of MLCCs were collected from a commercial charge–discharge platform (CFD-001, Gogo Instruments Technology, China).

## 3 Results and discussion

Figures 1(a) and 1(b) show the X-ray diffraction (XRD) patterns of the $(1-x)$BT–$x$BMNZZN ceramics. All the samples show the main perovskite structure of $BaTiO_3$, with trace amounts of the secondary phase $Ba_2Ti_5O_{12}$ (PDF#17-0661) detected at very low intensities, as indicated by (※). With increasing BMNZZN, all the XRD peaks shift to lower angles, which is related to the larger compound ion ($Mg_{0.2}Ni_{0.2}Zn_{0.2}Zr_{0.2}Nb_{0.2}$) ($R(Mg^{2+})$ = 0.72 Å, $R(Ni^{2+})$ = 0.69 Å, $R(Zn^{2+})$ = 0.74 Å, $R(Zr^{4+})$ = 0.72 Å, and $R(Nb^{5+})$ = 0.64 Å) replacing $Ti^{4+}$ (0.605 Å) in the B-site lattice [18]. The enlarged (200) peaks shown in Fig. 1(b) have no signs of splitting, indicating a high degree of symmetry in the solid solution [19]. Rietveld refinements of XRD patterns for $x$ = 0.08, 0.12, 0.16, and 0.20 using the tetragonal phase (T-phase, *P4mm* space group) and cubic phase (C-phase, $Pm\bar{3}m$ space group), with the results depicted in Fig. 1(c) and Fig. S1 in the Electronic Supplementary Material (ESM). The refinements exhibit good agreement with the experimental data, with low $R_{wp}$, $R_p$, and $\chi^2$ values of less than 7.12%, 4.75%, and 7.27, respectively [20,21]. The refinement indicates that within the range of $x$ = 0.08–0.20, both the T- and C-phases coexist. For $x$ = 0.16, the T-phase (*P4mm*) and C-phase ($Pm\bar{3}m$) contents are 27.02% and 72.98%, respectively.

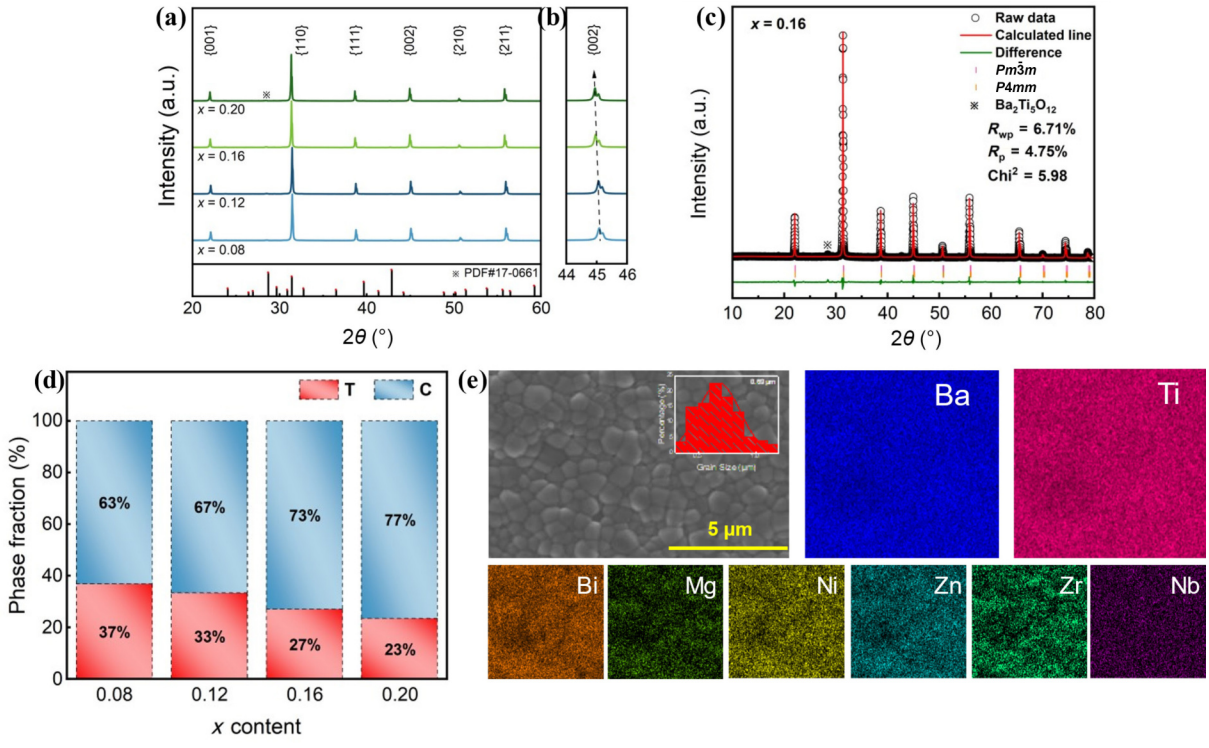


**Fig. 1** (a, b) XRD patterns of (1−*x*) BT–*x*BMNZZN ceramics; (c) Rietveld refinement pattern of 84BT–16BMNZZN ceramics where $R_{wp}$ is the weighted profile *R*-factor, $R_p$ is the profile *R*-factor, and $\chi^2$ is the Chi-squared; (d) T-phase and C-phase contents of (1−*x*) BT–*x*BMNZZN ceramics; (e) SEM images and EDS mapping images of 0.84BT–0.16BMNZZN ceramics.

Additionally, throughout the studied range of *x*, the concentration of the C-phase gradually increases, as shown in Fig. 1(d). Figure 1(e) and Fig. S2 in the ESM present scanning electron microscopy (SEM) images of the (1−*x*)BT–*x*BMNZZN ceramics. All the ceramics exhibited a dense microstructure with distinct grain boundaries and no apparent porosity. The grain size distributions are shown in the inset figures of Fig. 1(e) and Fig. S2 in the ESM, indicating that the average grain size decreased from 1.22 μm to 0.86, 0.69, and 0.64 μm for $x$ = 0.08, 0.12, 0.16, and 0.20, respectively, which is conducive to achieving high breakdown strength [22]. The results of energy-dispersive X-ray spectroscopy (EDS) are shown in Fig. 1(e) to characterize the elemental distribution. The elements in the 0.84BT–0.16BMNZZN ceramic, including Ba, Ti, Bi, Mg, Ni, Zn, Zr, and Nb, are uniformly distributed, suggesting the successful dissolution of BMNZZN into the BT matrix.

To gain deeper insights into the local structural variations in the (1−*x*)BT–*x*BMNZZN ceramics as a function of the BMNZZN content, Raman spectra were acquired and are presented in Fig. 2(a). The spectral features below 200 $cm^{-1}$ are associated with the vibrational modes of A-site cations. The peaks within the 200–450 $cm^{-1}$ range are attributed to B–O bond vibrations, whereas those above 450 $cm^{-1}$ correspond to the vibrational modes of $BO_6$ octahedra [23–25]. Notably, there is no discernible sharp peak at approximately 306 $cm^{-1}$, which is typically indicative of a "silent" mode of $B_1$+E(LO+TO) and is only observed in the presence of a long-range ferroelectric phase [26]. Concurrently, the $\nu_3$ peak at approximately 257 $cm^{-1}$ broadens with increasing *x*, as depicted in Fig. 2(b). These findings suggest that incorporating BMNZZN enhances structural disorder within the BT matrix, thereby disrupting long-range ferroelectric polarization. In Fig. 2(c), an increase in the BMNZZN concentration results in a redshift of the $\nu_1$ peak and a broadening of the Raman peak above 450 $cm^{-1}$, indicating significant local disorder due to valence mismatches among multiple cations occupying the A and B sites, resulting in smaller polar nanoregions and enhanced relaxor behavior [12,27,28].

The dark-field transmission electron microscopy (DF-TEM) pattern of the sample of $x$ = 0.16 is recorded in Fig. 2(d) to understand the evolution of the local structure. Long-range ferroelectric domains with large lamellar-shaped structures cannot be observed. High-angle annular dark-field (HAADF) STEM images acquired from the [100] direction were used to investigate specific atomic-scale effects of the BMNZZN composition, as shown in Fig. 2(e). The A-site and B-site cations appear as bright and dark spots, respectively, in the STEM images. The relative displacement of the central B-site cation concerning the corner A-site cations indicates the local polarization state, as indicated by the yellow arrows. The results indicate the formation of polarization nanoregions with dimensions of approximately 2–5 nm. To delve deeper into the PNRs and their dynamic response to an applied electric field, local poling experiments were performed via piezoelectric response force microscopy (PFM). Figure 2(f) and Fig. S3 in the ESM show the out-of-plane PFM images of the $x$ = 0.08, 0.12, 0.16, 0.20 ceramics after polarization treatment with ±20 V on a 2 μm × 2 μm square surface at different relaxation times. Upon removal of the external field, the PFM signals decay more rapidly with increasing *x*, suggesting that the domains revert more easily to their initial state, which is consistent with the characteristic behavior of relaxors [29,30]. The rapid reversibility of nanosized domains (such as PNRs) results in minimal $P_r$, thereby increasing the energy storage density and efficiency.

The unipolar *P*-*E* loops of (1−*x*)BT–*x*BMNZZN ceramics measured at 200 kV·$cm^{-1}$ are shown in Fig. 3(a). As the *x* content increases, the saturation polarization experiences a delay, and the

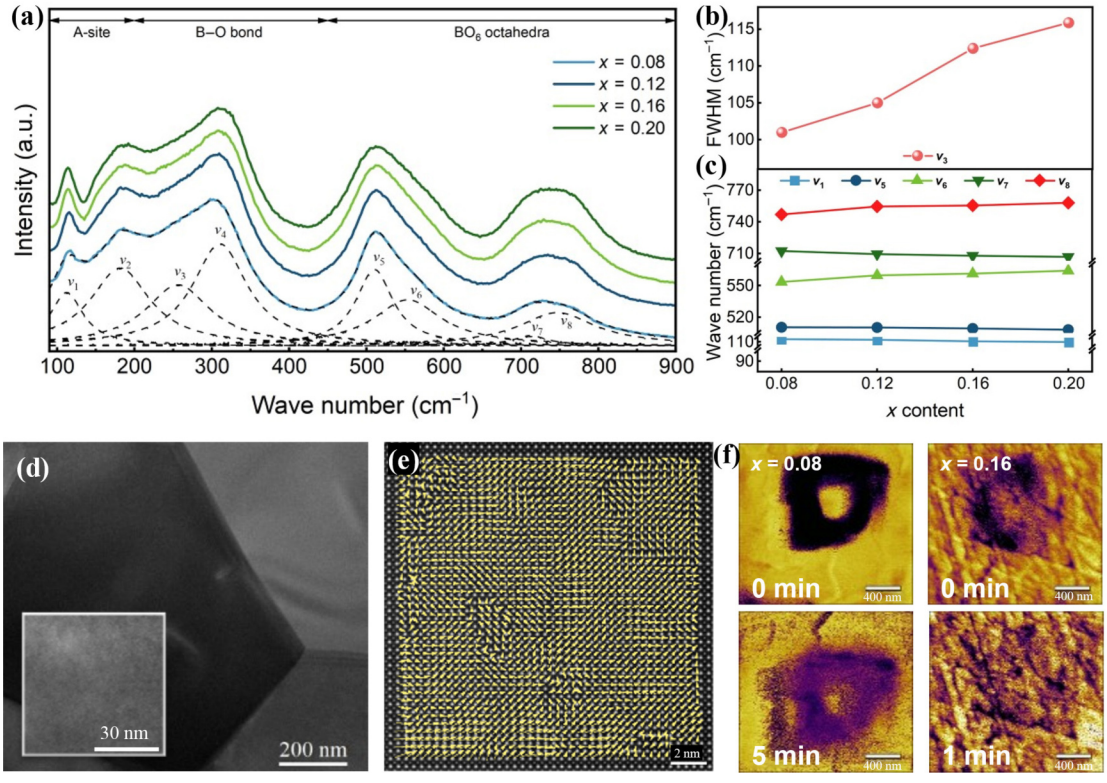


**Fig. 2** (a) Raman spectra of (1–*x*)BT–*x*BMNZZN ceramic samples at room temperature; (b) FWHM for $v_3$ peak and (c) variation in peak site; (d) DF-TEM micrographs for 0.84BT–0.16BMNZZN sample; (e) atomic-resolution HAADF-STEM polarization vector image along [100] direction of 0.84BT–0.16BMNZZN sample; (f) PFM phase pictures of $x = 0.08$ and 0.16 ceramics above a voltage of 20 V.

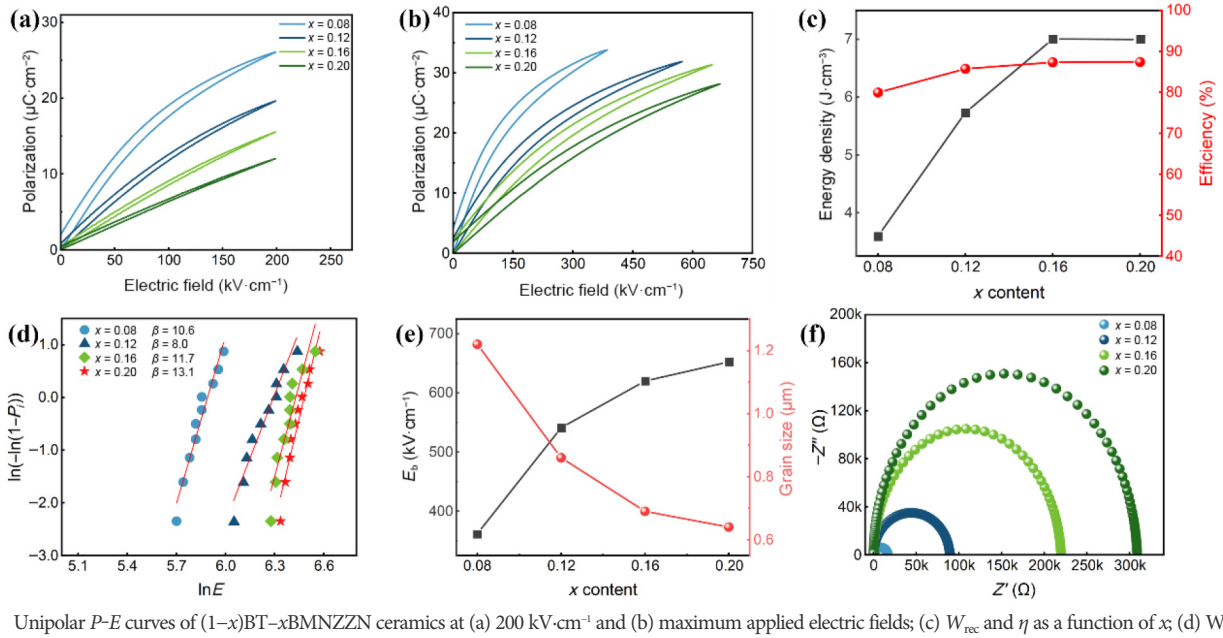


**Fig. 3** Unipolar *P*–*E* curves of (1–*x*)BT–*x*BMNZZN ceramics at (a) 200 kV·cm$^{-1}$ and (b) maximum applied electric fields; (c) $W_{rec}$ and $\eta$ as a function of *x*; (d) Weibull distribution of (1–*x*)BT–*x*BMNZZN ceramics; (e) change in $E_b$ and grain size vs. content of *x*; (f) impedance data of (1–*x*)BT–*x*BMNZZN ceramics at 600 °C.

*P*–*E* loops exhibit a nearly linear form, suggesting the disruption of long-range order in the ferroelectric state. Figure 3(b) shows the unipolar *P*–*E* loops of (1–*x*)BT–*x*BMNZZN ceramics measured at their respective maximum applied electric fields, with the results for $W_{rec}$ and $\eta$ presented in Fig. 3(c). Both $W_{rec}$ and $\eta$ increase with increasing *x*. At an electric field of 649 kV·cm$^{-1}$, the 0.84BT–0.16BMNZZN ceramic has the highest $W_{rec}$ of 7.0 J·cm$^{-3}$ and $\eta$ of 87.3%. The breakdown strength is a key parameter for determining the energy storage density of ceramic capacitors. The critical $E_b$ value and its reliability can be evaluated via the following formula: $X_i = \ln E_i$, $Y_i = \ln\{\ln(1/(1-P_i))\}$, $P_i = i/(n+1)$, where $E_i$ represents the breakdown field value of the *i*th sample, and *n* is the total number ($n = 10$). As depicted in Fig. 3(d), all samples exhibit good linear fit, with $\beta$ values greater than 8, indicating reliable Weibull distribution results and stable sample quality [31]. Additionally, $E_b$ increases gradually from

361.7 kV·cm$^{-1}$ ($x$ = 0.08) to 652.6 kV·cm$^{-1}$ ($x$ = 0.20), suggesting that the incorporation of BMNZZN enhances the breakdown strength, primarily because of the ability of BMNZZN to refine grains. Figure 3(e) illustrates the relationship between $E_b$ and the grain size. A smaller grain size inhibits the formation of a space charge layer at the grain boundary, leading to a higher $E_b$ [22,32,33]. Figure 3(f) shows the impedance data of the (1−$x$)BT–$x$BMNZZN ceramics, where all samples exhibit a single semicircle in the complex impedance plot. Owing to grain refinement, the density of the grain boundaries increases significantly, resulting in a substantial increase in resistance. The increased resistance after BMNZZN modification indicates enhanced insulation performance and improved breakdown strength.

The temperature-dependent dielectric constant ($\varepsilon_r$ vs. $T$) and loss (tan$\delta$ vs. $T$) over a temperature range of −100–200 °C are illustrated in Figs. 4(a) and 4(b) and Fig. S4 in the ESM. As the BMNZZN content increased, the dielectric peak broadened and diminished significantly. The room temperature dielectric constant at 1 kHz decreases from 1709 to 1422, 958, and 892 for $x$ = 0.08, 0.12, 0.16, and 0.20, respectively. Below $T_m$, all the compositions exhibit frequency dispersion, characteristic of relaxor ferroelectric behavior. The diffusivity coefficient ($\gamma$) was fitted at 100 kHz via the modified Curie–Weiss equation: $(1/\varepsilon_r) - (1/\varepsilon_m) = (T - T_m)^\gamma/C$, where $\varepsilon_m$ is the maximum $\varepsilon_r$ at $T_m$ , and $C$ is the Curie–Weiss constant, as shown in Fig. S4 in the ESM. The relaxation coefficient of all the samples exceeded 1.7, indicating strong relaxation properties in the (1−$x$)BT–$x$BMNZZN ceramic system. Figure 4(c) depicts the temperature coefficient of capacitance (TCC) variations for the (1−$x$)BT–$x$BMNZZN ceramics. Notably, TCC of the (1−$x$)BT–$x$BMNZZN ceramics ($x$ = 0.16 and 0.20) remains within ±15% across the temperature range of −55–200 °C, conforming to the X9R capacitor standard for temperature stability and demonstrating promising potential for multilayer ceramic capacitor applications.

To further improve the energy storage performance, a 0.84BT–0.16BMNZZN composition with superior polarization compared with 0.80BT–0.20BMNZZN was chosen for the fabrication of MLCCs. Consequently, five-layer 0.84BT–0.16BMNZZN MLCCs were produced via tape casting, and an optical image of a 0.84BT–0.16BMNZZN MLCCs measuring 2.8 mm × 2.8 mm × 0.4 mm (length × width × height) is depicted in Fig. 5(a). SEM and EDS images of the 0.84BT–0.16BMNZZN MLCCs are presented in Figs. 5(b) and 5(c), revealing a layer thickness of approximately 7.4 μm. The distinct interface between the 0.84BT–0.16BMNZZN layer and the Pt layer is evident, with the Pt electrode appearing flat and continuous. The unipolar $P$–$E$ loop of the 0.84BT–0.16BMNZZN MLCCs is shown in Fig. 5(d). As the applied electric field increases from 644 to 1614 kV·cm$^{-1}$, $P_{max}$ of 0.84BT–0.16BMNZZN MLCCs increases from 20.8 to 29.4 μC·cm$^{-2}$, whereas $P_r$ remains low (< 1 μC·cm$^{-2}$). The reduction in $P_{max}$ compared with ceramics can be attributed to the clamping effect [34] and challenges in precisely determining the electrode area or dielectric thickness for buried electrodes [35]. The energy storage properties are illustrated in Fig. 5(e). As the applied electric field intensifies, $W_{rec}$ of 0.84BT–0.16BMNZZN MLCCs increases from 4.9 J·cm$^{-3}$ (@644 kV·cm$^{-1}$) to 15.7 J·cm$^{-3}$ (@1614 kV·cm$^{-1}$), maintaining an efficiency above 95% across the entire electric field range. The Weibull distribution fitting lines and $E_b$ values for the 0.84BT–0.16BMNZZN MLCCs sample are shown in Fig. 5(f), where the shape parameter $\beta$ exceeds 19, confirming the statistical reliability and stability of the sample. Figure 5(g) compares the $E_b$, $W_{rec}$, and $\eta$ values among the 0.92BT–0.08BMNZZN ceramics, 0.84BT–0.16BMNZZN ceramics, and 0.84BT–0.16BMNZZN MLCCs. The incorporation of BMNZZN notably enhances $E_b$ in ceramic samples. Reducing the dielectric layer thickness to 7.4 μm yields an $E_b$ value of 1580 kV·cm$^{-1}$ in the 0.84BT–0.16BMNZZN MLCCs, representing a 155% increase over that of bulk ceramics. Thus, $W_{rec}$ of 0.84BT–0.16BMNZZN MLCCs is substantially increased by approximately 125% compared with that of the 0.84BT–0.16BMNZZN ceramics. Additionally, the increased $\eta$ of the 0.84BT–0.16BMNZZN MLCCs may be attributed to its multilayer structure design and the low applied voltage during testing. Figure 5(h) contrasts the 0.84BT–0.16BMNZZN MLCCs with other lead-free MLCCs [12–14,34,36–44], demonstrating ultrahigh $W_{rec}$ of 15.7 J·cm$^{-3}$ and ultrahigh $\eta$ of 96.4% for lead-free BT-based MLCCs, underscoring the significant application potential of 0.84BT–0.16BMNZZN MLCCs.

The development of MLCCs capable of reliable operation over a broad temperature range and exhibiting high energy storage performance is essential for meeting the requirements of environments with fluctuating temperature conditions. The unipolar $P$–$E$ loops of the 0.84BT–0.16BMNZZN MLCCs subjected to an electric field of 1078 kV cm$^{-1}$ at various temperatures are depicted in Figs. 6(a) and 6(b). The 0.84BT–0.16BMNZZN MLCCs demonstrates excellent temperature stability within the temperature range of −12–100 °C, with variations in $W_{rec}$ and $\eta$ being less than 4.85% and 9.33%, respectively. Furthermore, in situ Raman spectroscopy was conducted on 0.84BT–0.16BMNZZN ceramics to elucidate the underlying mechanism of their superior temperature stability. As illustrated in Fig. 6(c), a continuous Raman peak is observed from −120 to 200 °C, with no emergence of new peaks as the temperature increases, suggesting that the ceramic does not undergo a structural phase transition and retains its structure up to 200 °C [24,45,46]. With increasing temperature, the intensity of

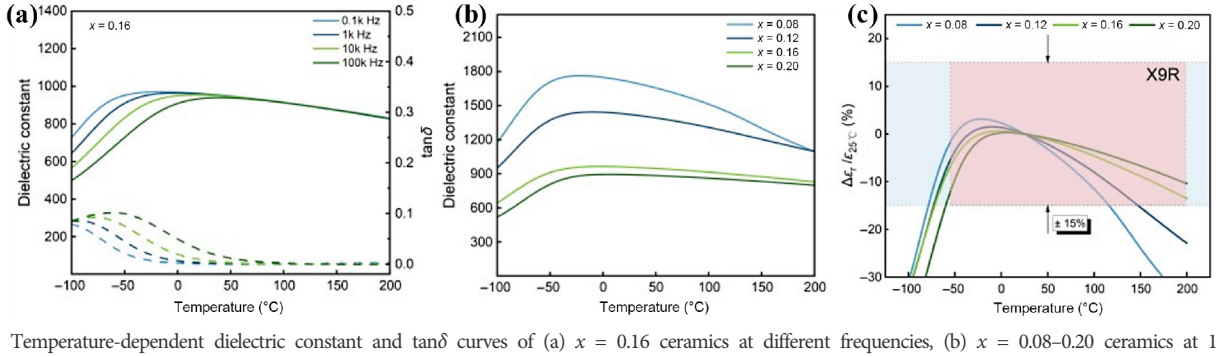


**Fig. 4** Temperature-dependent dielectric constant and tan$\delta$ curves of (a) $x$ = 0.16 ceramics at different frequencies, (b) $x$ = 0.08–0.20 ceramics at 1 kHz, and (c) temperature coefficient of capacitance values of (1−$x$)BT–$x$BMNZZN ceramics.


清華大学出版社 Tsinghua University Press | SciOpen

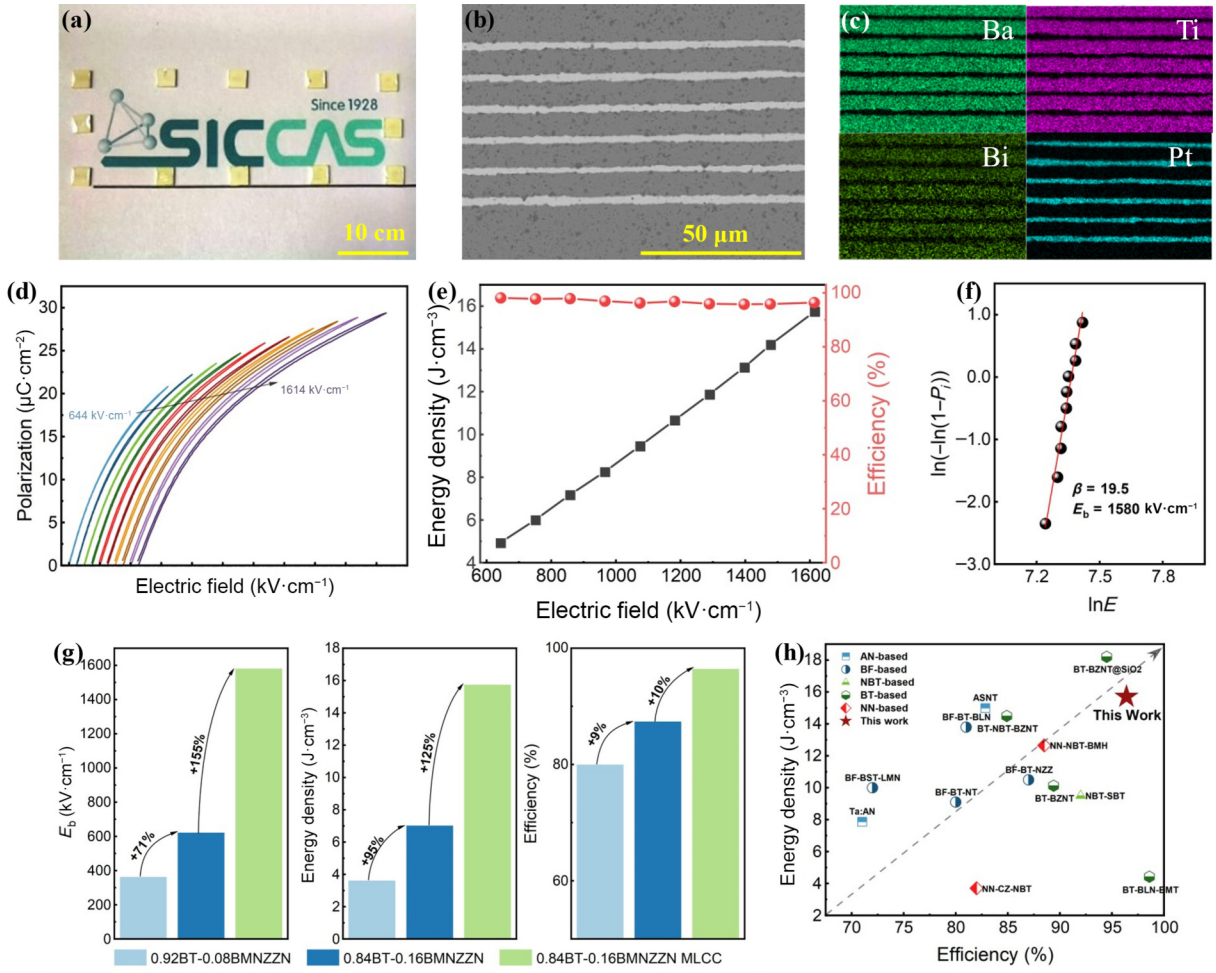


**Fig. 5** (a) Optical photo of 0.84BT–0.16BMNZZN MLCCs; (b) SEM images and (c) EDS mapping images of 0.84BT–0.16BMNZZN MLCCs; (d) unipolar *P*–*E* curves for 0.84BT–0.16BMNZZN MLCCs under different applied electric fields; (e) $W_{rec}$ and $\eta$ of 0.84BT–0.16BMNZZN MLCCs; (f) Weibull distribution of 0.84BT–0.16BMNZZN MLCCs; (g) comparison of $E_b$, $W_{rec}$, and $\eta$ values between 0.92BT–0.08BMNZZN/0.84BT–0.16BMNZZN ceramics and 0.84BT–0.16BMNZZN MLCCs. (h) $W_{rec}$ and $\eta$ of 0.84BT–0.16BMNZZN MLCCs compared with those of other lead-free MLCCs.

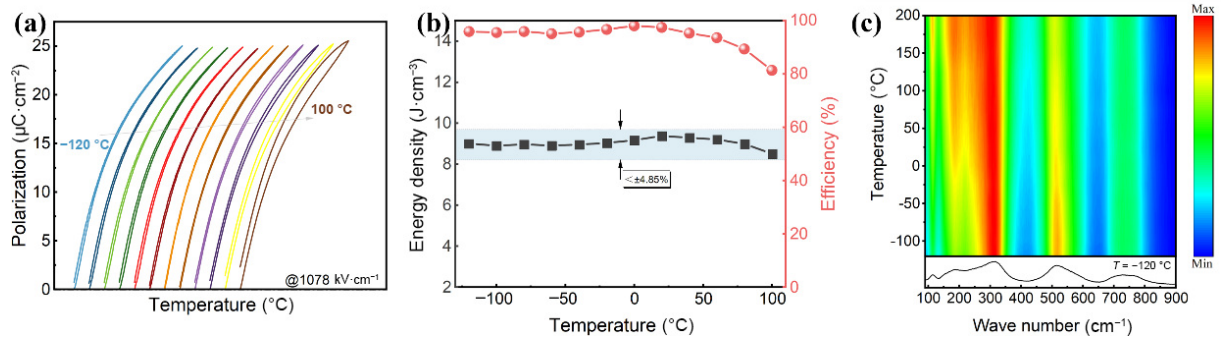


**Fig. 6** (a) Unipolar *P*–*E* curves of 0.84BT–0.16BMNZZN MLCCs measured at different temperatures (−120–100 °C), (b) $W_{rec}$ and $\eta$ values of 0.84BT–0.16BMNZZN MLCCs as functions of temperature, and (c) temperature-dependent Raman spectra of 0.84BT–0.16BMNZZN ceramic.

the $BO_6$ modes decreases and shifts to a lower wavenumber, indicating a reduction in the vibration and relaxation of the B-O chain motion, which is consistent with the behavior of most RFE ceramics. The broadening of the Raman peak is attributed to the high activity of PNRs, which contributes to the temperature stability of the energy storage performance of the RFE ceramics [43].

The frequency and cycle reliability of the 0.84BT–0.16BMNZZN MLCCs were assessed by measuring its unipolar *P*–*E* loop at 1078 kV·cm$^{-1}$ and room temperature across various cycles and frequencies. Figure S5 in the ESM shows that the *P*–*E* loop remains consistent under different conditions, highlighting the excellent fatigue resistance and frequency stability of the material. The variations in $W_{rec}$ and $\eta$ concerning the number of cycles and frequency are depicted in Figs. 7(a) and 7(b). Over $10^7$ cycles and frequencies ranging from 10 to 250 Hz, the fluctuations in $W_{rec}$ were 0.82% and 0.92%, respectively, underscoring the broad applicability of 0.84BT–0.16BMNZZN MLCCs.

The underdamped charge–discharge characteristics of the 0.84BT–0.16BMNZZN MLCCs are illustrated in Figs. 7(c) and 7(d). As the electric field intensifies, the initial current peak

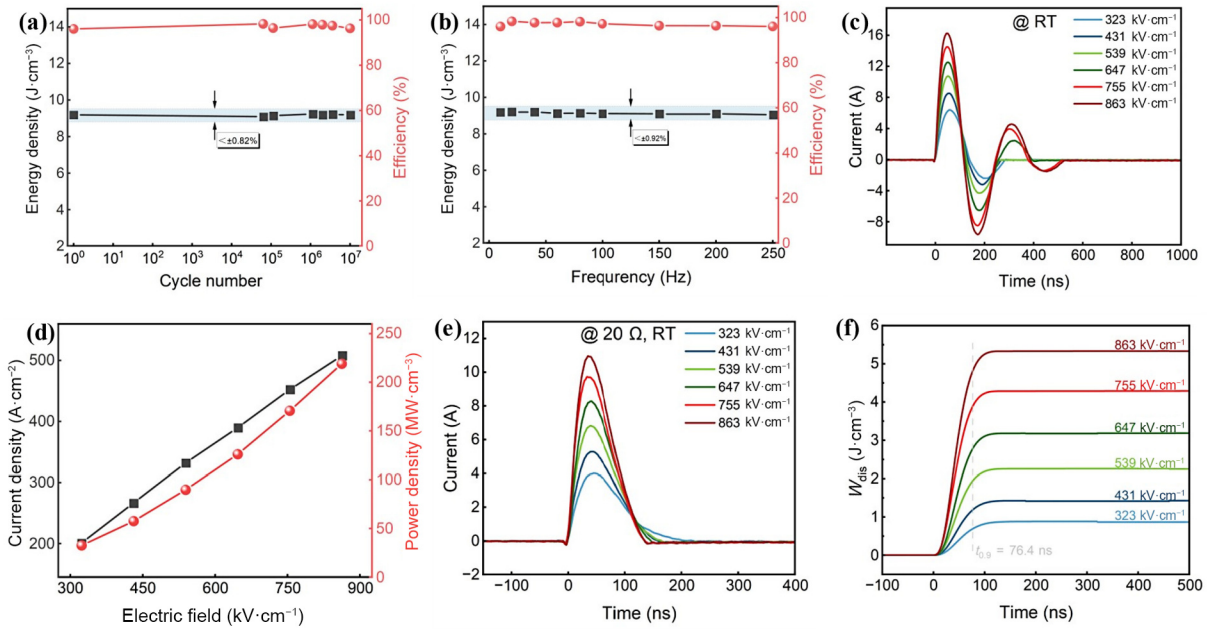


**Fig. 7** (a) $W_{rec}$ and $\eta$ of 0.84BT–0.16BMNZZN MLCCs during $10^7$ cycles; (b) variation in $W_{rec}$ and $\eta$ for 0.84BT–0.16BMNZZN MLCCs with frequency; (c) underdamped discharge waveforms (RT refers to room temperature) and (d) $C_D$ and $P_D$ for 0.84BT–0.16BMNZZN MLCCs under varying electric fields; (e) overdamped discharge curves; (f) $W_{dis}$ of 0.84BT–0.16BMNZZN MLCCs as a function of time with constant load resistance.

progressively increases. At 863 kV·cm$^{-1}$, the maximum current ($I_{max}$), current density ($C_D$), and power density ($P_D = EI_{max}/(2S)$; where $S$ represents the electrode area of the tested sample) reached 16.5 A, 507.7 A·cm$^{-2}$, and 219 MW·cm$^{-3}$, respectively. The discharge energy density ($W_{dis}$) was calculated via the equation $W_{dis} = R\int (I^2(t)\,dt/V)$ [46]. According to Figs. 7(e) and 7(f), $W_{dis}$ of 5.3 J·cm$^{-3}$ was achieved at 863 kV·cm$^{-1}$. Additionally, at an electric field strength of 863 kV·cm$^{-1}$, the time required to release 90% of the stored energy, denoted as $t_{0.9}$, is approximately 76.4 ns, indicating an extremely fast discharge rate. Additionally, 0.84BT–0.16BMNZZN MLCCs demonstrated excellent stability in terms of charge–discharge performance across the temperature range of 25–130 °C, as illustrated in Fig. S6 in the ESM. In summary, 0.84BT–0.16BMNZZN MLCCs demonstrates extensive application potential in advanced high-power/pulse power systems because of its superior fatigue resistance, frequency stability, high power density, and rapid discharge rate.

## 4 Conclusions

In this study, we simultaneously achieved ultrahigh $W_{rec}$ of 15.7 J·cm$^{-3}$ and ultrahigh $\eta$ of 96.4% in BT-based MLCCs through the integration of a high-entropy strategy and a multilayer structure in the 0.84BT–0.16BMNZZN MLCCs. The incorporation of the high-entropy component BMNZZN into the BT matrix not only facilitates the formation of polar nanoregions to enhance the relaxation performance but also reduces the grain size, thereby improving the breakdown strength. Furthermore, a multilayer ceramic structure with a reduced dielectric layer thickness (~7.4 μm) was fabricated via a tape casting process, which further increased $E_b$. Notably, the 0.84BT–0.16BMNZZN MLCC demonstrated excellent temperature stability (< ±4.85%) over the range of −120–100 °C, frequency stability (< ±0.82%) across 10–250 Hz, and fatigue resistance (< ±0.92%) for up to $10^7$ cycles. These findings underscore the potential of the BT–BMNZZN system as a promising lead-free alternative for energy storage applications.

## Acknowledgements

This work received funding from the Natural Science Foundation of Shanghai (Grant No. 21ZR1473100) and the National Natural Science Foundation of China (Grant Nos. U2002217, 51831010, and 5227130). We would like to thank Dr. Tengfei Hu and Associate Researcher Zhengqian Fu for their assistance with the High-angle annular dark-field (HAADF) STEM tests.

## Declaration of competing interest

The authors have no competing interests to declare that are relevant to the content of this article.

## Electronic Supplementary Material

Supplementary material is available in the online version of this article at https://doi.org/10.26599/JAC.2024.9221018.

## References

[1] Sun Z, Zhang J, Luo HJ, *et al.* Superior capacitive energy-storage performance in Pb-free relaxors with a simple chemical composition. *J Am Chem Soc* 2023, **145**: 6194–6202.

[2] Li JL, Shen ZH, Chen XH, *et al.* Grain-orientation-engineered multilayer ceramic capacitors for energy storage applications. *Nat Mater* 2020, **19**: 999–1005.

[3] Kim J, Saremi S, Acharya M, *et al.* Ultrahigh capacitive energy density in ion-bombarded relaxor ferroelectric films. *Science* 2020, **369**: 81–84.

[4] Pan H, Lan S, Xu SQ, *et al.* Ultrahigh energy storage in superparaelectric relaxor ferroelectrics. *Science* 2021, **374**: 100–104.

[5] Pan H, Li F, Liu Y, *et al.* Ultrahigh-energy density lead-free dielectric films *via* polymorphic nanodomain design. *Science* 2019, **365**: 578–582.

[6] Hu D, Pan ZB, Tan XY, *et al.* Optimization the energy density and efficiency of $BaTiO_3$-based ceramics for capacitor applications. *Chem Eng J* 2021, **409**: 127375.

[7] Wei XK, Domingo N, Sun Y, *et al.* Progress on emerging ferroelectric materials for energy harvesting, storage and conversion. *Adv Energy Mater* 2022, **12**: 2201199.

[8] Zhao PY, Cai ZM, Wu LW, *et al.* Perspectives and challenges for lead-

free energy-storage multilayer ceramic capacitors. *J Adv Ceram* 2021, **10**: 1153–1193.
[9] Ji HF, Wang DW, Bao WC, *et al.* Ultrahigh energy density in short-range tilted NBT-based lead-free multilayer ceramic capacitors by nanodomain percolation. *Energy Storage Mater* 2021, **38**: 113–120.
[10] Yao FZ, Yuan QB, Wang Q, *et al.* Multiscale structural engineering of dielectric ceramics for energy storage applications: From bulk to thin films. *Nanoscale* 2020, **12**: 17165–17184.
[11] Liu ZG, Li MD, Tang ZH, *et al.* Enhanced energy storage density and efficiency in lead-free $Bi(Mg_{1/2}Hf_{1/2})O_3$–modified $BaTiO_3$ ceramics. *Chem Eng J* 2021, **418**: 129379.
[12] Li WB, Zhou D, Liu WF, *et al.* High-temperature $BaTiO_3$-based ternary dielectric multilayers for energy storage applications with high efficiency. *Chem Eng J* 2021, **414**: 128760.
[13] Zhao PY, Wang HX, Wu LW, *et al.* High-performance relaxor ferroelectric materials for energy storage applications. *Adv Energy Mater* 2019, **9**: 1803048.
[14] Zhao PY, Cai ZM, Chen LL, *et al.* Ultra-high energy storage performance in lead-free multilayer ceramic capacitors via a multiscale optimization strategy. *Energy Environ Sci* 2020, **13**: 4882–4890.
[15] Yang BB, Zhang Y, Pan H, *et al.* High-entropy enhanced capacitive energy storage. *Nat Mater* 2022, **21**: 1074–1080.
[16] Chen L, Deng SQ, Liu H, *et al.* Giant energy-storage density with ultrahigh efficiency in lead-free relaxors via high-entropy design. *Nat Commun* 2022, **13**: 3089.
[17] Qiao WJ, Xu ZZ, Yuan WZ, *et al.* High-performance energy storage in BNST-based lead-free ferroelectric ceramics achieved through high-entropy engineering. *Chem Eng J* 2023, **477**: 147167.
[18] Shannon RD. Revised effective ionic radii and systematic studies of interatomic distances in halides and chalcogenides. *Acta Cryst A* 1976, **32**: 751–767.
[19] Li D, Xu DM, Zhao WC, *et al.* A high-temperature performing and near-zero energy loss lead-free ceramic capacitor. *Energy Environ Sci* 2023, **16**: 4511–4521.
[20] Huan Y, Gui DY, Li CX, *et al.* Simultaneously enhanced energy storage performance and luminance resistance in $(K_{0.5}Na_{0.5})NbO_3$-based ceramics via synergistic optimization strategy. *J Adv Ceram* 2024, **13**: 34–43.
[21] Tian A, Zuo RZ, Qi H, *et al.* Large energy-storage density in transition-metal oxide modified $NaNbO_3$–$Bi(Mg_{0.5}Ti_{0.5})O_3$ lead-free ceramics through regulating the antiferroelectric phase structure. *J Mater Chem A* 2020, **8**: 8352–8359.
[22] Yan F, Zhou XF, He X, *et al.* Superior energy storage properties and excellent stability achieved in environment-friendly ferroelectrics via composition design strategy. *Nano Energy* 2020, **75**: 105012.
[23] Yang F, Li Q, Zhang A, *et al.* High energy storage density and temperature stable dielectric properties of $(1-x)Bi_{0.5}(Na_{0.82}K_{0.18})_{0.5}Ti_{0.99}(Y_{0.5}Nb_{0.5})_{0.01}O_{3-x}NaNbO_3$ ceramics. *J Alloys Compd* 2022, **925**: 166782.
[24] Kang RR, Wang ZP, Liu WY, *et al.* Domain engineered lead-free ceramics with large energy storage density and ultra-high efficiency under low electric fields. *ACS Appl Mater Interfaces* 2021, **13**: 25143–25152.
[25] Yuzyuk YI. Raman scattering spectra of ceramics, films, and superlattices of ferroelectric perovskites: A review. *Phys Solid State* 2012, **54**: 1026–1059.
[26] Long CB, Zhou WJ, Song HM, *et al.* Simultaneously realizing ultrahigh energy storage density and efficiency in $BaTiO_3$-based dielectric ceramics by creating highly dynamic polar nanoregions and intrinsic conduction. *Acta Mater* 2023, **256**: 119135.
[27] He JH, Feng Q, Huang HX, *et al.* The effect of A-site Mg substitution on energy-storage density and efficiency of $Bi_{0.47}Na_{0.47}Ba_{0.06}TiO_3$ ceramics by disordered induction. *Ceram Int* 2024, **50**: 3334–3343.
[28] Li Y, Liu Y, Tang MY, *et al.* Energy storage performance of $BaTiO_3$-based relaxor ferroelectric ceramics prepared through a two-step process. *Chem Eng J* 2021, **419**: 129673.
[29] Dong XY, Li X, Chen HY, *et al.* Realizing enhanced energy storage and hardness performances in $0.90NaNbO_3$–$0.10Bi(Zn_{0.5}Sn_{0.5})O_3$ ceramics. *J Adv Ceram* 2022, **11**: 729–741.
[30] Peng HN, Liu Z, Fu ZQ, *et al.* Superior energy density achieved in unfilled tungsten bronze ferroelectrics via multiscale regulation strategy. *Adv Sci (Weinh)* 2023, **10**: 2300227.
[31] Wang M, Feng Q, Luo CY, *et al.* Ultrahigh energy storage density and efficiency in $Bi_{0.5}Na_{0.5}TiO_3$-based ceramics *via* the domain and bandgap engineering. *ACS Appl Mater Interfaces* 2021, **13**: 51218–51229.
[32] Cai ZM, Wang XH, Hong W, *et al.* Grain-size–dependent dielectric properties in nanograin ferroelectrics. *J Am Ceram Soc* 2018, **101**: 5487–5496.
[33] Tunkasiri T, Rujijanagul G. Dielectric strength of fine grained barium titanate ceramics. *J Mater Sci Lett* 1996, **15**: 1767–1769.
[34] Zhu LF, Zhao L, Yan YK, *et al.* Composition and strain engineered $AgNbO_3$-based multilayer capacitors for ultra-high energy storage capacity. *J Mater Chem A* 2021, **9**: 9655–9664.
[35] Ogihara H, Randall CA, Trolier-McKinstry S. High-energy density capacitors utilizing $0.7BaTiO_3$–$0.3BiScO_3$ ceramics. *J Am Ceram Soc* 2009, **92**: 1719–1724.
[36] Zhao MY, Wang J, Zhang J, *et al.* Ultrahigh energy storage performance realized in $AgNbO_3$-based antiferroelectric materials *via* multiscale engineering. *J Adv Ceram* 2023, **12**: 1166–1177.
[37] Li JL, Li F, Xu Z, *et al.* Multilayer lead-free ceramic capacitors with ultrahigh energy density and efficiency. *Adv Mater* 2018, **30**: 1802155.
[38] Zhu LF, Yan YK, Leng HY, *et al.* Energy-storage performance of $NaNbO_3$ based multilayered capacitors. *J Mater Chem C* 2021, **9**: 7950–7957.
[39] Zhu LF, Song AZ, Zhang BP, *et al.* Boosting energy storage performance of $BiFeO_3$-based multilayer capacitors via enhancing ionic bonding and relaxor behavior. *J Mater Chem A* 2022, **10**: 7382–7390.
[40] Wang G, Lu ZL, Yang HJ, *et al.* Fatigue resistant lead-free multilayer ceramic capacitors with ultrahigh energy density. *J Mater Chem A* 2020, **8**: 11414–11423.
[41] Wang G, Lu ZL, Li JL, *et al.* Lead-free $(Ba,Sr)TiO_3$–$BiFeO_3$ based multilayer ceramic capacitors with high energy density. *J Eur Ceram Soc* 2020, **40**: 1779–1783.
[42] Wang G, Li JL, Zhang X, *et al.* Ultrahigh energy storage density lead-free multilayers by controlled electrical homogeneity. *Energy Environ Sci* 2019, **12**: 582–588.
[43] Lv ZQ, Lu T, Liu Z, *et al.* $NaNbO_3$-based multilayer ceramic capacitors with ultrahigh energy storage performance. *Adv Energy Mater* 2024, **14**: 2304291.
[44] Zhao PY, Chen LL, Li LT, *et al.* Ultrahigh energy density with excellent thermal stability in lead-free multilayer ceramic capacitors via composite strategy design. *J Mater Chem A* 2021, **9**: 25914–25921.
[45] Zhu CQ, Cai ZM, Luo BC, *et al.* High temperature lead-free BNT-based ceramics with stable energy storage and dielectric properties. *J Mater Chem A* 2020, **8**: 683–692.
[46] Deng T, Liu Z, Hu TF, *et al.* Excellent energy-storage performance in $Bi_{0.5}Na_{0.5}TiO_3$-based lead-free composite ceramics via introducing pyrochlore phase $Sm_2Ti_2O_7$. *Chem Eng J* 2023, **465**: 142992.